Silicon Nanoparticles: Are they Crystalline from the Core to the Surface?

Alyxandra N. Thiessen, [§] Michelle Ha, [§] Riley W. Hooper, Haoyang Yu, Anton O. Oliynyk, Jonathan G. C. Veinot, and Vladimir K. Michaelis**

Department of Chemistry, University of Alberta, Edmonton, Alberta, Canada, T6G 2G2

ABSTRACT

Silicon nanoparticles (SiNPs) are biologically compatible, metal-free quantum dots that exhibit size and surface tailorable photoluminescence. The nanostructure of these materials influences their optical, chemical, and material properties and hence plays an important role in their future-generation applications in sensors, battery electrodes, optical materials and contrast agents, among others. In this work, we employ a complement of methods including X-ray photoelectron spectroscopy (XPS), bright-field transmission electron microscopy (TEM), powder X-ray diffraction (XRD), Fourier transform infrared spectroscopy, and ^{29}Si solid-state nuclear magnetic resonance (NMR) spectroscopy to interrogate the bulk structure of hydride-terminated SiNPs (H-SiNPs) ranging from 3 to 64 nm in diameter and effectively probe their surface. By applying these methods, we have demonstrated that H-SiNPs consist of a size dependent layered structure made up of surface, subsurface, and core silicon regimes. The surface silicon species are manifested as a broad underlying feature in the corresponding ^{29}Si NMR spectra between -80 to -120 ppm for small nanoparticles (NPs), whereas the sharp resonance at lower frequency (*ca.* -80.9 ppm, 1 ppm full-width at half maximum) present in large NPs is attributed to the well-ordered crystalline silicon core. A critical size junction has been identified for H-SiNPs, where XPS and NMR show features arising from surface, subsurface, and core silicon species are present for 9 nm NPs. This structural insight provides essential understanding and potential advancement in the development of SiNP-based applications in photovoltaic, battery anodes, and sensors.

INTRODUCTION

Semiconductor nanoparticles (i.e., quantum dots; QDs) exhibit exquisitely tunable optoelectronic properties that make them useful for a variety of applications including displays, photovoltaics, and sensors. Unfortunately, many QDs are based upon toxic constituents (e.g., Cd) that are regulated in many jurisdictions.[1] In this context, identifying, preparing, and tailoring the properties of toxic-metal-free (TMF) QDs is of paramount importance. Silicon nanoparticles (SiNPs) are TMF QDs that are readily prepared using abundant materials;[2, 3] they possess tailorable surface chemistry, exhibit size- and surface chemistry-tunable photoluminescence that spans the visible and near-infrared spectral regions with absolute quantum yields that compete with their CdSe-based counterparts,[4, 5] possess long-lived (microsecond) excited states,[6] are biologically compatible,[2, 7] and reversibly alloy with lithium. As such, SiNPs are being explored as functional materials in luminescence-based biological imaging,[3, 8] medical imaging,[9, 10] light-emitting diodes,[11] photovoltaics,[12-14] sensors,[15] solar concentrators,[16] and lithium ion battery anodes.[17-19] For many of these applications, SiNP size and surface profoundly impact material performance.[20] For example, when employed in lithium ion battery anodes, the SiNP surface has been implicated in the formation of the solid electrolyte interphase layer that drastically impacts device performance.[19, 21] Similarly, the SiNP surface plays an important role in defining their optical properties (e.g., luminescent color, brightness, photoluminescence (PL) quantum yield, excited state lifetime); by defining the surface bonded moiety, the SiNPs PL can be tuned through the visible range and the excited state lifetime can be defined within the micro- to nano-second regime.[22-24] Furthermore, various ill-defined surfaces (e.g., defects, oxidation, etc.) have been implicated in low SiNP PL quantum yields.[5, 25]

In light of their key roles in material properties, understanding the SiNP surface and internal structure is of paramount importance. Approaches to probing SiNP surfaces have been multifaceted. Quantum chemical calculations provide insight into the nature of the SiNP-oxide interface for oxide-

embedded NPs.[26-28] These modeling studies suggest that, when embedded in oxides, SiNPs possess a strained structure that leads to the formation of species such as distorted (i.e., elongated or shortened) Si-Si bonds, dangling bonds, coordination defects, and Si-O-Si bridging species.[26, 27, 29] The surfaces of SiNPs have also been interrogated directly using various spectroscopic methods. Raman spectroscopy provides direct probing of Si-Si bonds;[30-32] multiple Si-Si species have been identified for small particles (d ~ 3 nm) and as the particle size is increased, features associated with surface species disappear.[30] Fourier transform infrared spectroscopy (FTIR) also provides information regarding bonding in SiNP surface species, including Si-H_x, Si-O, and Si-*R* (*R*=alkyl, aryl, etc.);[33-36] however, due to dipole considerations, FTIR does not directly probe Si-Si bonding.

Nuclear magnetic resonance (NMR) spectroscopy is a workhorse method for molecular and materials characterization; ^{1}H NMR spectroscopy has been applied, in combination with other methods (e.g., Raman, FTIR, etc.) to evaluate SiNP surface derivatization.[4, 37-46] It, as well as ^{19}F NMR spectroscopy, have also been used to indirectly probe the speciation of surface functionalities on hydride-terminated SiNPs (H-SiNPs) via the evaluation of reaction byproducts.[4] Solid-state NMR spectroscopy is a powerful analytical method that provides data related to atomic-level short- and medium-range structural differences within nanomaterials.[47] Despite suffering from a low natural abundance (4.7%), ^{29}Si is an NMR-active nucleus with a nuclear spin, I = ½, a moderate Larmor frequency (19.9% that of ^{1}H), and chemical shift range. These combined properties result in relatively narrow linewidths and good resolution for solids when using magic-angle spinning (MAS) and allow for identification of a variety of silicon species. To date, applications of solid-state NMR spectroscopy for SiNP evaluation have been largely confined to functionalized,[37-43, 45, 48] ammonium/chloride capped,[44, 49] doped,[50] porous,[46, 51] nanoclusters,[52] or micron-sized high polarization studies,[9, 53] while non-doped hydride-terminated studies are less prevalent,[54-56] due in part to their reactivity and limited solution processibility. Previously a combination of cross-

polarization and single-pulse methods with strategic wetting aided in decoding various Si-based surface species on d ~ 50 nm SiNPs;[54] this approach was quickly expanded to assess the impact of surface functionalization.[55] These examples, and others,[57-65] demonstrate the wide-ranging utility of NMR spectroscopy and its applicability to a diverse array of Si-based nanomaterials.

In this regard, size-dependent ^{29}Si NMR analyses of SiNPs is expected to provide invaluable insight into their structure that may be used to optimize material performance in far reaching applications. In this work, we describe a methodical investigation of H-SiNPs with predefined dimensions ranging from 3 to 64 nm, employing a complementary suite of characterization methods including X-ray photoelectron spectroscopy (XPS), FTIR spectroscopy, bright-field transmission electron microscopy (TEM), powder X-ray diffraction (XRD), and ^{29}Si solid-state NMR spectroscopy that reveals the size dependent order/disorder within the NPs. We further elucidate an intermediate layer, denoted here as the *subsurface*, using cross-polarization NMR spectroscopy and SiNP size dependent nuclear spin-lattice relaxation behavior.

EXPERIMENTAL SECTION

MATERIALS

Starting Materials

Hydrofluoric (Electronic grade, 48–50%) and sulfuric (reagent grade, 95–98%) acids were purchased from Fisher Scientific and Caledon Laboratory Chemicals, respectively. Fuming sulfuric acid (reagent grade, 20% free SO_3 bases), trichlorosilane (99%) and toluene (HPLC grade) were purchased from Sigma-Aldrich. Toluene was purified using a Pure-Solv purification system and collected immediately prior to use. Benzene was purchased from EMD Millapore (now Millapore Sigma). All reagents and solvents were used as received unless otherwise specified.

Preparation of Hydrogen Silsesquioxane (HSQ)

HSQ was synthesized following a modified literature procedure.[66] Briefly, dry toluene (45.0 mL) was added to a mixture of concentrated (15.0 mL) and fuming (7.2 mL) sulfuric acid under an inert atmosphere. A second solution of dry toluene (110 mL) and trichlorosilane (16 mL) was prepared and added drop-wise to the sulfuric acid mixture over a few hours. The toluene layer was isolated and washed with sulfuric acid solution. After drying the organic layer over $MgSO_4$ (neutralized with $CaCO_3$ overnight), the volume was initially reduced using a rotary evaporator and then evaporated to dryness *in vacuo* to yield the desired product as a white solid that was stored under vacuum until use.

Preparation of the H-SiNPs

Thermally induced disproportionation of the HSQ was exploited to produce the well-defined SiNPs used in this study.[67] Briefly, six grams of HSQ was thermally processed in a standard tube furnace under flowing 5% H_2/95% Ar at 1100, 1200, 1300, 1400, or 1500 °C. This procedure yielded oxide composites containing SiNPs of predefined sizes ranging from 3 to 64 nm. The resulting composites containing SiNPs were ground using an agate mortar and pestle followed by shaking in a wrist action shaker with high purity glass beads for six hours.

The resulting powder was etched using a 1:1:1 solution of ethanol:deionized water:HF to liberate the H-SiNPs; a typical etching procedure employed ~1 g and 30 mL of composite and etching solution, respectively. The composite was exposed to the etching solution for one hour after which H-SiNPs were extracted into toluene and isolated by centrifugation. The H-SiNPs were then subjected to two suspension/centrifugation cycles in toluene followed by dispersion in benzene for freeze-drying. The benzene suspension was freeze dried to obtain a free-flowing H-SiNP powder. Samples were packed into ZrO_2 NMR rotors and sealed with Kel-F drive caps. Identical samples were also evaluated using FTIR, XPS, and bright-field TEM. All material manipulations were performed in a nitrogen-filled dry box to ensure negligible surface oxidation or reaction with water.

CHARACTERIZATION

Fourier Transform Infrared Spectroscopy (FTIR)

FTIR was performed on a Thermo Nicolet Continum FT-IR microscope by drop casting SiNPs onto a silicon wafer from dry toluene suspensions.

X-ray Photoelectron Spectroscopy (XPS)

XPS was measured using a Kratos Axis 165 Ultra X-ray photoelectron spectrometer. A monochromatic Al K_α source operating at 140 W with an energy $h\nu$ = 1486.6 eV was used. Survey spectra were collected with an analyzer pass energy of 160 eV and steps of 0.3 eV (Figure S1). For high-resolution spectra, the pass energy was 20 eV and the step was 0.1 eV with a dwell time of 200 ms. Samples were prepared by drop-coating a dry toluene dispersion of SiNPs onto a copper foil. Spectra were calibrated to the aliphatic C component of the C 1s binding energy of adventitious carbon (284.8 eV)[68, 69] and fit to appropriate spin-orbit pairs using CasaXPS (VAMAS) software taking into account a Shirley-type background. To fit the Si 2p high-resolution spectrum, the spin-orbit couple doublet area ratio was fixed at 2:1 and the peak-to-peak separation was defined to be 0.62 eV (Figure S2). The spectral window was fit using a variant of a literature procedure.[70] Briefly,

the spectral components (i.e., spin-orbit couple doublet) arising from elemental Si (near 99.4 - 99.5 eV in this work) were fit first using a symmetric Gaussian-Lorentzian line shape for small-size particles. When splitting was observed in the envelope shape (i.e., d ~ 9, 21, and 64 nm), a Lorentzian asymmetric (LA) line shape was applied (LA(1.93, 3.2, n) where n defines the Gaussian width).[71] To account for the decreased structural order with SiNPs arising from decreased particle size, the full-width at half maximum (FWHM) of the spectral components used to fit the elemental Si features were constrained as follows (d, FWHM): 3nm, 1.13 eV; 6 nm, 0.93 eV; 9 nm, 0.63 eV; 21 nm, 0.6 eV; 64 nm, 0.58 eV. The residual area was always fit using a Gaussian-Lorentzian line shape with the same doublet relationship noted above.

Transmission Electron Microscopy (TEM)

TEM imaging was performed using a JEOL-2010 electron microscope equipped with a LaB_6 source and an accelerating voltage of 200 kV. Specimens were prepared by drop-casting toluene suspensions of H-SiNPs onto carbon-coated copper grids. The NP size was determined by averaging the size of 300 particles using ImageJ software (version 1.51j8), Figure S3. Bright field images of d ~ 3 nm SiNPs showed substantial aggregation making imaging impractical for sizing the material. To overcome this, d ~ 3 nm H-SiNPs were functionalized with dodecene using established thermally-induced hydrosilylation and subsequently imaged.[72]

Powder X-ray Diffraction (XRD)

Lyophilized samples were placed on a zero-background Si wafer. XRD data were acquired using a Rigaku XRD Ultima IV equipped with a Cu K_α radiation source. Data for H-SiNPs with TEM-determined sizes 64, 21, 9, 6, and 3 nm were analyzed using a series of diffraction line-broadening methods (i.e., integral breadth, FWHM, and Lorentzian broadening) to determine crystallite sizes. Material properties, as well as instrumental factors contribute to diffraction peak line broadening. Instrumental effects were accounted for by refining a NIST LaB_6 standard to ensure instrument

alignment and a Si standard was used as an infinitely large crystallite size reference (Figure S4). After subtraction of instrumental contribution, line broadening was assumed to result only from size/strain effects. The patterns were analyzed and fit using the TOPAS Academic software package.[73]

Solid-state NMR Spectroscopy

Silicon-29 NMR spectra were obtained at 9.39 T (ν_0 (^{1}H) = 399.95 MHz, ν_0 (^{29}Si) = 79.46 MHz) on a Bruker Avance III HD 400 NMR spectrometer. All data were acquired using a 4 mm double-resonance (H-X) Bruker MAS NMR probe. To ensure that samples had not degraded during analysis, all samples were checked pre- and post-NMR analysis using XPS and FTIR. All NMR data were acquired under magic-angle spinning conditions at ambient temperature with a spinning frequency of 10 ± 0.002 kHz. The data for all experiments were acquired using TPPM[74] ^{1}H decoupling ($\gamma B_1/2\pi$ = 62.5 kHz). ^{29}Si NMR data were referenced to TMS (δ = 0) by setting the high frequency peak of tetrakistrimethylsilylsilane to −9.8 ppm.[75] All spectral deconvolutions were performed with Origin 2018, T_1 data were fit within MATLAB 2017 assuming mono- or bi-exponential recoveries, and NMR data were processed within TOPSPIN using between 50 and 200 Hz Lorentizan broadening. Unless otherwise noted, data were collected with at least 5 × T_1 of the longest measured T_1 time.

Analysis of H-SiNP Surface and Core: Direct excitation ^{29}Si MAS NMR data were acquired using a Bloch[76] pulse with a 4 μs $\pi/2$ pulse ($\gamma B_1/2\pi$ = 62.5 kHz), optimized recycle delays (below) between 3.3 minutes and 24 hours, and between 4 and 2048 co-added transients.

Analysis of the H-SiNP Surface: Cross-polarization[77] (CP) ^{29}Si[^{1}H] MAS NMR data were acquired with a 4 μs $\pi/2$ pulse ($\gamma B_1/2\pi$ = 62.5 kHz) on ^{1}H, ramped Hartman-Hahn match on ^{29}Si, 5 ms contact time, 10 s recycle delay and between 7776 and 10240 co-added transients.

Deconvolution of H-SiNP Surface/Subsurface: The contact time was varied from 0.05 to 8 ms to further elucidate spectral changes in the CP MAS data, as longer contact times provide time for

nuclear spin diffusion to propagate further into the particle. A two-dimensional $^{29}Si[^{1}H]$ HETCOR spectrum was obtained on the 64 nm particle using 1024 co-added transients, 3 ms contact time (conditions identical to CP experiments above) and 16 t_2 increments.

Nuclear Spin-Lattice Relaxation: Spin-lattice ^{29}Si relaxation data were acquired using the saturation recovery[78] experiment with a pre-saturation train of 16 pulses and a 4 μs π/2 pulse ($\gamma B_1/2\pi$ = 62.5 kHz) and 1 - 1024 co-added transients. For the smaller NPs, the relaxation delay was varied from 0.5 to 1000 s (Table 1 and S5), but for the 21 and 64 nm NPs, very large relaxation times rendered this approach impractical. Thus, for these two samples, the ^{29}Si nuclei were saturated with a series of short pulses, followed by a very long delay (up to 144 h) prior to acquisition of a single free induction delay.

RESULTS AND DISCUSSION

Solid-state NMR spectroscopy is an ensemble technique that probes comparatively large quantities of material (i.e., tens to hundreds of mgs) and provides information regarding local structure and dynamics. If nanomaterial structural-property relationships are to be elucidated from such investigations, it is imperative that the NP size, shape, and composition be as uniform as possible to allow effective differentiation/identification of the nuclear environments that are present. To achieve this for SiNPs, we have prepared SiNP/SiO_2 composites that contain nanoscale inclusions of silicon with pre-defined sizes using a well-established, scalable method involving the thermal processing of HSQ;[6, 67, 79] high-quality freestanding H-SiNPs are routinely liberated from these composites via alcoholic HF etching. In most cases, H-SiNPs are rendered solution processable and resistant toward oxidation upon surface derivatization using various approaches (e.g., hydrosilylation).[40, 80-85] The focus of this study is to investigate the internal SiNP structure free from the influences of surface functionalities; H-SiNPs provide the nearest approximation to 'naked' SiNPs available outside ultrahigh vacuum environments.

X-ray photoelectron spectroscopy is an information rich method that provides data related to material composition and the constituent element chemical environment (e.g., oxidation state, nearest neighbor bonding environment, etc.). The survey spectra of the present H-SiNPs were calibrated to the aliphatic C 1s signal of adventitious carbon. These data indicate that all specimens contain only Si, C, O, and F (Figure S1). Fluorine impurities, arising from the alcoholic HF etching procedure that liberates H-SiNPs from the composite, cannot be avoided. Close examination of the C 1s high-resolution XP spectra shows evidence of substantial oxygen-containing carbon species (i.e., C-O, C=O, O-C=O, etc.; Figure S2). The relative ratios of these carbon-containing components are consistent for all sizes of H-SiNPs and are correlated with the amount of oxygen detected in the respective samples (Figure S1). From these analyses we conclude that the majority of the oxygen

within the present H-SiNP specimens resides within the adventitious carbon species and is not associated with H-SiNP oxidation. This conclusion is further supported by FTIR analyses (Figure S6) and the high-resolution Si 2p spectra (Figures 1a and S2) that are readily deconvolved into Si 2p 3/2 and Si 2p 1/2 spin-orbit couples. For all H-SiNPs, the energy separation of these doublets was fixed at 0.62 eV, and the Si 2p 1/2 to Si 2p 3/2 area was fixed at 0.50. For small H-SiNPs (d ~ 3 and 6 nm), all components (including minor oxide contributions denoted in green) were fit to a Voigt GL(30) line shape (70% Gaussian; 30% Lorentzian). The rationale for applying this fitting procedure lies in the nature of the NP sizes investigated. If NPs are small enough (<9 nm for the SiNPs in the current study), a considerable number of atoms experience slightly different (disordered) chemical environments (see NMR discussion below) that lead to a distribution of binding energies and symmetric broadening that is Lorentzian in nature. As a result, the overall observed signal is dominated by a symmetric Gaussian/Lorentzian line shape. For the largest SiNPs (d ~ 21 and 64 nm) that represent bulk silicon (see XRD and NMR below), the spectral envelope was fit using a Lorentzian asymmetric line shape LA(a,b,n), where *a* and *b* define the asymmetry and *n* defines the Gaussian width. Similar procedures have been employed when fitting the Si 2p data of bulk crystalline silicon.[71] The d ~ 9 nm H-SiNPs lie within an intermediate size regime where it is possible to isolate the surface and core Si contributions to the Si 2p emission. The Si 2p spectrum of these H-SiNPs was effectively fit by first applying the procedure noted for large NPs (highlighted in red in Figures 1a and S2) and the remaining residual signal arising from surface atoms was fit using a GL (30) line shape (highlighted in blue). Of important note, the binding energy of the surface silicon species is shifted to higher energy as a result of electronegativity considerations arising because of bonding interactions with surface hydride moieties (i.e., SiH_x).

TEM imaging of H-SiNPs can be exceptionally challenging because of their limited electron contrast and poor solution processability. NP dimensions determined from bright-field TEM imaging

(Figure S3) are summarized in Table 1. All H-SiNPs were readily imaged with the exception of d ~ 3 nm H-SiNPs, which were heavily agglomerated. To determine the size of these NPs, it was necessary to render them solution processable by modifying their surfaces with dodecyl moieties using standard non-size selective thermally-induced hydrosilylation (Figure 1b); functionalized NPs obtained from the identical composites used to prepare those evaluated in our NMR studies showed a TEM-derived diameter of 3.5 ± 0.9 nm.

Table 1: Particle Band Gap and Size Analysis from TEM and XRD

Nominal (nm)	Annealing Temp. (∘C)	Band gap (eV)[b]	TEM (nm)	XRD (nm)[c]
3	1100	1.57	3.5 ± 0.9	1.2 ± 0.1
6	1200	1.33	5.5 ± 1.2	2.5 ± 0.1
9	1300	1.22	8.7 ± 1.2	4.7 ± 0.2
21	1400	1.14	20.7 ± 4.0	10.2 ± 0.3
64	1500	1.12	64.0 ± 16.9	22.4 ± 0.2
[a]microcrystalline	-	1.12	44 x 10^3	-

a. Bulk microcrystalline (44 micron) silicon (Aldrich)
b. Band gap determined from the method described by Wheeler et al.[25]
c. Values determined from powder X-ray diffraction using the integral breadth method[86]

It is well-established that X-ray powder diffraction peak broadening provides an indirect method for approximating nanocrystal/crystallite size that is complementary to direct TEM imaging. After instrumental contributions are accounted for, only size and strain factors remain. It is possible to qualitatively identify these contributions by considering the dependence of peak broadening on diffraction angle; size-induced broadening follows a 1/(cos(θ)) relationship while strain-induced broadening follows a tan(θ) trend. For the present NPs, the broadening distribution (i.e., FWHM) shows what is expected for size-induced broadening (Figure S7) with deviations arising from strain contributions being noted for smaller particles (d ~ 3 and 6 nm). In this context, the peak fits were refined appropriately taking into account size-dependent strain contributions. Diffraction peak geometry was successfully fit using a pseudo-Voight function. A polynomial background was also

included and no over-fitting (absolute correlation) was found for all polynomial terms. In addition, it was necessary to include a synthetic peak 22° to effectively describe the peak shapes of the 3 nm particle diffraction pattern. Finally, all diffraction data were analyzed using integral breadth, FWHM, and Lorentzian broadening methods that all assume a normal distribution of spherical crystallites.[86] A straightforward comparison of TEM and XRD derived data (Figure 1, Table 1) shows that TEM determined dimensions of H-SiNPs are consistently larger; this is not surprising, and is consistent with present XPS and NMR analyses, given XRD peak broadening only gives a volume-average distribution of crystallite sizes that are routinely smaller than the size of the entire NP (i.e., XRD analyses only probe the crystalline portion of NPs).

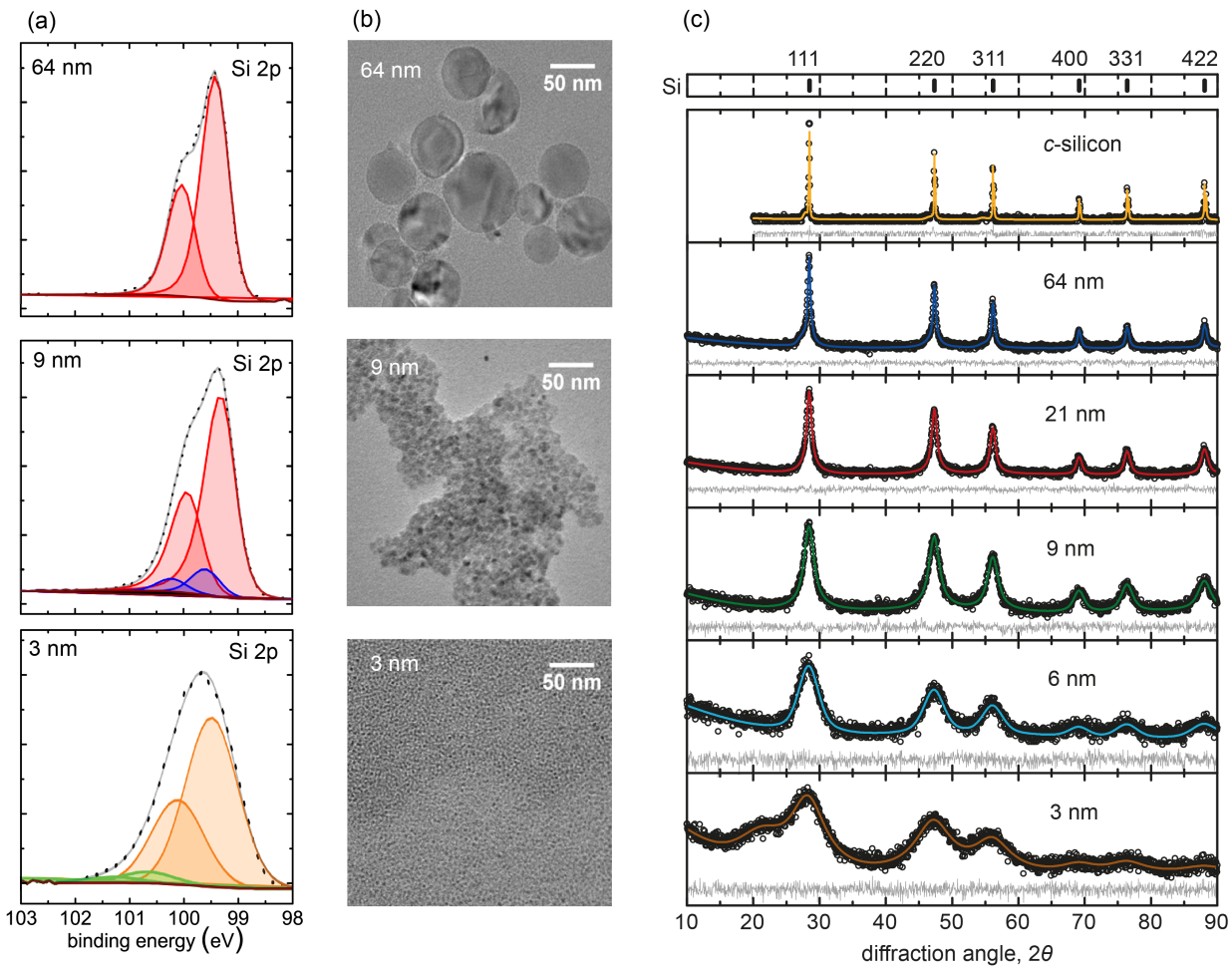

Figure 1: (a) High-resolution Si 2p XPS showing the 2p3/2 emission for 64, 9, and 3 nm H-SiNPs (the Si 2p1/2 component was omitted for clarity). The colored traces correspond to: grey = experimental data, dotted black = complete fit, red = crystalline core Si, blue = surface Si, orange = disordered Si, and green = Si oxides. (b) Bright-field TEM images of H-SiNPs (d ~ 64 and 9 nm) and dodecyl-SiNPs (d ~ 3 nm). (c) XRD patterns for d ~ 64 (blue), 21 (red), 9 (green), 6 (cyan), and 3 (brown) nm H-SiNPs, showing characteristic Si 111, 220, 311, 400, 331, and 422 reflections.

To further evaluate the H-SiNPs, direct excitation (surface and core) and cross polarization (surface) ^{29}Si MAS NMR spectroscopy was employed. Figure 2 shows the direct ^{29}Si MAS NMR data revealing a considerable evolution from ultrahigh resolution (1 ppm, FWHM) for microcrystalline silicon to a broad resonance spanning nearly 40 ppm, from −75 to −120 ppm, for the 3 nm particles. Peak positions and linewidths in the ^{29}Si NMR spectra are consistent with size-dependent changes in the atomic and/or electronic structure of the NPs. The center-of-gravity

chemical shift (δ_{cgs}) of amorphous silicon (*a*-Si*)* has been reported to be −41 ± 3 ppm (with a Gaussian-like resonance that spans 40 to −130 ppm); crystalline (*c*-Si) silicon appears at lower frequency (isotropic chemical shift, δ_{iso} = −80.9 ± 1 ppm; 1 ppm FWHM).[87-90] In this context, we attribute the sharp resonance appearing at −81 ppm to *c*-Si (i.e., the material possesses a highly ordered structure); this feature shifts to lower frequency with decreasing particle dimensions from 44 μm to 21 nm. As the NP size decreases to below 10 nm a broad resonance emerges, eventually replacing the sharp *c*-Si resonance that would be associated with highly-ordered silicon. We attribute this change in peak shape and breadth to an increased influence of surface states with decreasing NP size. Since the total surface area of the NPs increase as the dimensions decrease, the fraction of silicon atoms residing in disordered atomic positions increases (see below). These NP structural changes are manifested in the NMR spectra given the sensitivity of the ^{29}Si magnetic shielding to local atomic structure (variations in bond angles and lengths, defects caused by dangling bonds, variations in surface species (e.g., SiH_n where n = 1 to 3), and/or combinations thereof), and are consistent with conclusions based on previous Raman[30] spectroscopy results. Magnetic shielding can also be influenced by the local electronic structure, which is discussed further below. These effects are not unique to SiNPs and have been reported for numerous nanomaterials, including InP, Zn_3P_2, ZnSe, Cd, Na, Ag, Pb, etc.[47, 91-99]

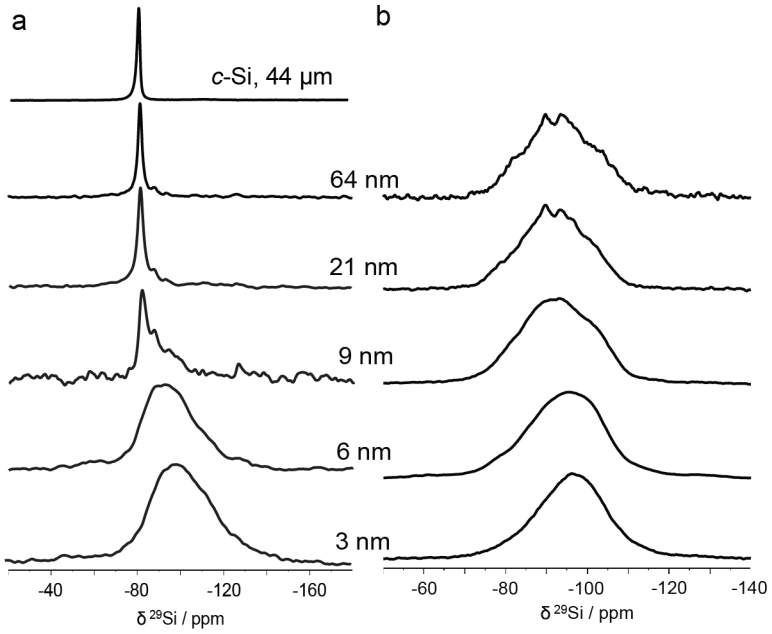

Figure 2: Direct (a) and CP (b) ^{29}Si MAS NMR spectra of H-SiNPs with varying particle diameters.

To further elucidate the origin of the apparent NP size dependent ^{29}Si chemical shift, linewidth, and shape, we employed a ^{29}Si[^{1}H] CP MAS NMR to selectively interrogate silicon atoms at the NP surface.[77, 100] This experiment depends on dipole interactions between ^{29}Si and ^{1}H nuclei and enhances signals arising from ^{29}Si nuclei in close proximity to hydrogen atoms (i.e., directly bonded or through space; *ca.* <10 Å). All CP MAS NMR spectra (Figure 2b, Figure S8) are broad (i.e., −80 to −120 ppm) and featureless for the smallest nanoparticles; features emerge as the NP size increases. Knowing hydride moieties are present on the SiNP surfaces (FTIR; Figure S6), we attribute the main broad resonances to surface Si-H_x species that experience substantial structural variability (local disorder). It is reasonable to assume that the Si atomic positions at the NP surfaces are ill-defined (i.e., the structure lacks long-range periodicity) and exist in a distribution of chemical environments (*vide supra*); doubtless the number of Si nuclei chemical environments is compounded by the presence of a distribution, however small it may be, of NP sizes in every sample (Table 1).[54-56, 101-104]

Closer examination of the spectra obtained for the smallest NPs (d ~ 3 and 6 nm) reveals a broad featureless, slightly asymmetric resonance centered at *ca.* −96 ppm. While crystalline and amorphous SiO_2 could appear within a similar chemical shift range (δ_{iso} ~ −110 ppm)[62, 105] our complementary XP analysis confirms that the amount of oxygen-bonded silicon is low (~ 0.7 to 6 atomic %) and FTIR shows no evidence of Si-bonded hydroxyl groups (e.g., Si-OH). Hence, if present, we contend that surface oxides contribute negligibly to the NMR spectra (d ~ 6 to 64 nm) and these features result from SiH_x species (Table S1 provides a summary of common ^{29}Si chemical shifts). One interesting feature worth noting is the slightly different features of the 3 nm particle, evident when overlaying the direct and CP ^{29}Si NMR data. An extra signal from the direct ^{29}Si NMR spectrum appears between −100 and −120 ppm, that does not have ^{1}H's nearby (as ^{29}Si nuclei will not be detected using the CP technique if there are no nearby ^{1}Hs). This may be due to a small amount of the Si surface being oxidized (< 7%, SiO_x) or the electronic structure further impacting the chemical shift of these high surface area particles which have a bandgap of ~1.6 eV. As a control illustrating the impact of oxygen on the spectra of H-SiNPs, we purposefully oxidized a sample over a period of months, revealing the formation of SiO_2 (Figure S9) and analyzes the SiNPs pre- and post-NMR analysis using XPS and FTIR (Figure S10).

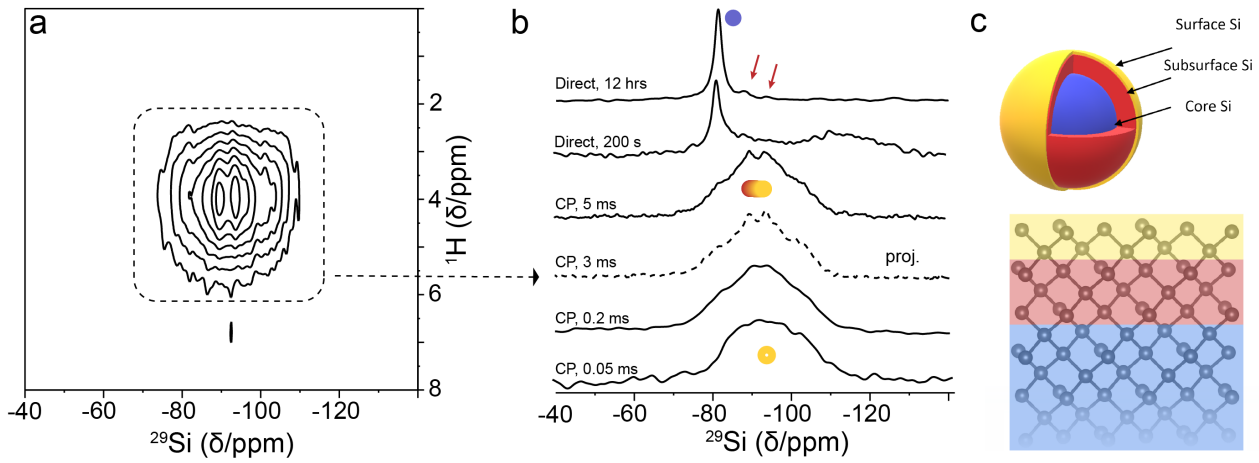

Figure 3: (a) Two-dimensional ^{29}Si[^{1}H] HETCOR MAS NMR spectra of 64 nm H-SiNPs with a mixing time of 3.0 ms. (b) Overlay of direct excitation ^{29}Si MAS NMR and ^{29}Si[^{1}H] CP MAS NMR with variable mixing times for 64 nm H-SiNP to illustrate NMR features corresponding to H-SiNP surface (yellow), subsurface (red), and core (blue) signatures. Red arrows indicate sharper subsurface NMR features present in the direct excitation ^{29}Si MAS NMR as seen with ^{29}Si[^{1}H] CP MAS NMR with a mixing time of 3.0 ms. Direct excitation ^{29}Si MAS NMR with a relatively short recycle delay of 200 s was used to artificially enhance the surface resonance still detectable with such short recycle delays. (c) Artistic schematic of a H-SiNP indicating the silicon surface, subsurface, and core with a model of the first ten atomic layers of H-SiNPs.

Turning our attention to the largest NPs considered here (d ~ 21 and 64 nm), they too exhibit a broad resonance with two superimposed sharp features. These features emerge in the 2D ^{29}Si[^{1}H] HETCOR spectrum (Figure 3a) and in the CP MAS NMR data (Figures 3b and S8) with longer contact times. Closer examination of the ^{29}Si MAS NMR data (Figures 3b and 2a) also confirms two new features in low intensity. Their appearance and increased intensity with longer mixing times suggests the presence of an intermediate or subsurface of quasi-ordered Si atoms. The ^{29}Si MAS NMR spectra of intermediate dimension H-SiNPs (d ~ 9 nm) show evidence of these two extremes (Figure 2a) consistent with the presence of three structural regimes within the NPs: a crystalline core, quasi-crystalline subsurface, and disordered surface (Figure 3c). Similar effects have been reported in other NPs including CeO_2 and noble metal nanomaterials.[99, 106]

Building on our understanding of the underlying structure of the presented H-SiNPs, we turn our attention to the NP size-dependence of the ^{29}Si chemical shift. A disturbance of the local nuclear

electronic environment about a given nucleus typically manifests itself in a change of the observed chemical shift. The magnetic shielding interaction[107-109] (chemical and/or Knight shift) could be responsible for the observed effect, depending upon the nanomaterial studied. Knight shifts dominate in metallic systems while SiNP semiconductors are impacted by diamagnetic and paramagnetic magnetic shielding contributions.[47, 109] Changes in the paramagnetic contributions can be rationalized by the size-dependence of the electronic excitation energy (ΔE),[98, 109] whereby decreasing NP size causes an increase in band gap (as the case for the SiNPs considered here). An increase in ΔE causes greater magnetic shielding and the ^{29}Si chemical shifts appearing at lower frequencies (Figure 4a).[47, 95, 98, 109-111] This general reasoning is often invoked when considering the NMR spectra of nanomaterials, originating from molecular systems that have appropriate molecular orbital symmetries.[107, 108] Therefore, the changes in δ_{cgs} observed for the samples studied here appear to be related to size-dependent electronic properties of SiNPs, and are expected to be continuous until the band gap reaches its bulk value of 1.12 eV (δ_{iso} of d ~ 64 nm ≈ bulk *c*-Si).

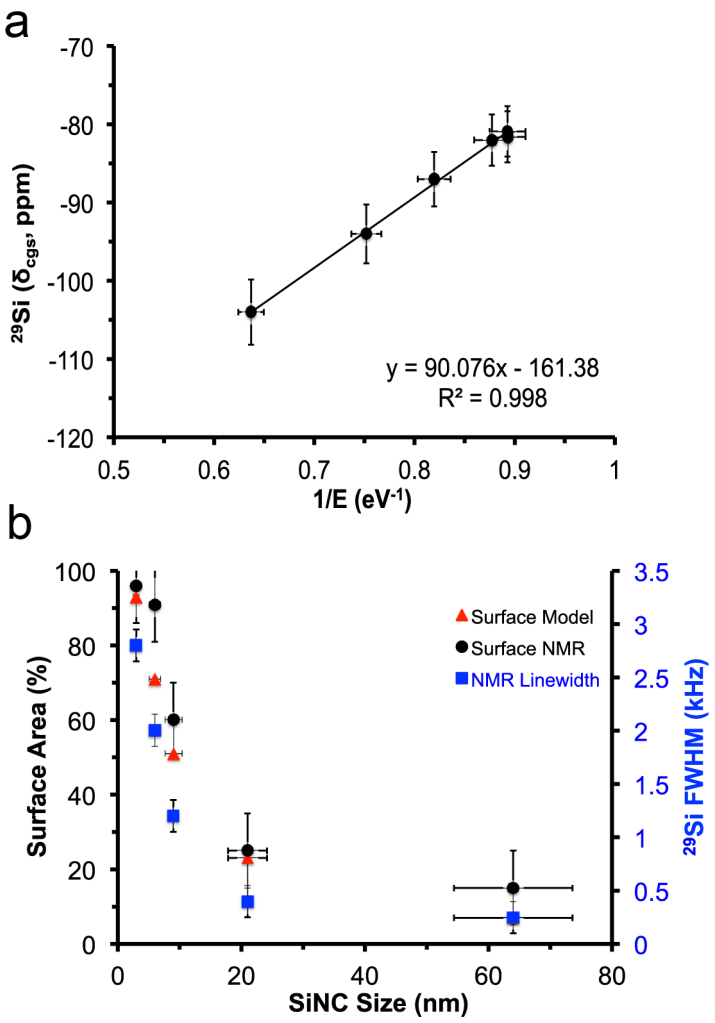

Figure 4: (a) Relationship between δ_{cgs} and the inverse bandgap of SiNPs. (b) Surface/subsurface area % derived from NMR data (black) and a model (red), as well as the ^{29}Si FWHM, blue, plotted as a function of H-SiNP size. As the H-SiNPs move from a disordered to ordered system, the corresponding surface area % and linewidth decrease as the NP size increases.

Another notable feature of the presented ^{29}Si NMR spectra is the broad underlying feature whose intensity is inversely related to NP size for dimensions ≤ 21 nm (Table 2). With decreasing NP diameter, the relative contribution from surface nuclei increases such that the contribution from the ordered core becomes minor (even negligible) for the smallest NPs - long-range order simply is not possible within the confines of such small NPs. Nevertheless, the factors discussed previously are still expected to play a role and give rise to a range of chemical shifts for nuclei at or near the surface.

These observations are consistent with the XRD data (Figure 1c): reflections broaden with decreasing size, as expected with a reduction in the number of repeat units in the NP, which results in structural strain and poorer coherence in the diffraction of the material.[112]

To investigate the impact of local structure on linewidth, we modeled and estimated (from the ^{29}Si MAS NMR data) the surface/subsurface volume as a function of particle size (Figure 4b and Table 2). The number of surface Si atoms on the H-SiNPs was calculated as a function of size based on an assumed icosahedral shape for all sizes except the 64 nm (where a spherical shape was invoked).[113, 114] This allowed us to estimate the number of surface/subsurface atoms (assuming four layers; 5 layers total including the surface) by removing one layer at a time from the surface; the values determined from this analysis are summarized in Table S2. Combining these estimates with the XRD data allows an assessment of the reduction in the size of the ordered bulk lattice with the formation of a disordered surface. With increasing surface area (decreasing NP size), the relative contribution of the ordered core atoms to the NMR spectra at ca. −81 ppm is reduced and no longer resolved for 3 and 6 nm NPs. These observations are consistent with the XRD and TEM particle size determination. Considering the unit cell length for crystalline silicon is 0.54 nm and the smallest particle investigated here has a diameter of 3.5 nm, only ~ 6 unit cell lengths would be needed for the particle cross section. This reinforces the complementary nature of both XRD (long-range) and NMR (short-range) for the study of materials that exhibit both structural order and local disorder. While we cannot discount the influence of quantum confinement, computational studies show that oxide-embedded 3 nm SiNPs have significant strain throughout the particle.[27] It would follow that this strain would manifest itself as defects including distorted Si-Si bonds, dangling bonds, and coordination defects that are delocalized around the surface of the SiNP, as outlined by Lee *et al.*[26] These defects limit long-range order in the nanoparticle as is evidenced by the extreme broadening of the XRD reflections and NMR spectra. Scherrer analysis of the XRD data reveals an average

crystallite size of 1.7 nm for 3 nm SiNPs, which correlates to just over three Si unit cell lengths,[115] lacking long-range structure.

Table 2: Experimental ^{29}Si MAS NMR FWHM, nuclear spin-lattice relaxation times (T_1) and surface fraction deconvolutions of the H-SiNPs with varying particle diameters.

Particle Size /nm	FWHM (± 10%)[a]	H-SiNC, T_1 /min		^{29}Si Surface Fraction /%	
	kHz	Surface	Core	NMR[c] (± 10%)	Model[d]
64	0.3	0.9 ± 0.1	158.2 ± 15.0	15	7
21	0.5	3.8 ± 0.4	102.1 ± 10.1	25	23
9	1.2	1.3 ± 0.1	6.9 ± 0.7	60	51
6	2.1	5.8 ± 0.6[b]		91	71
3	2.8	1.4 ± 0.1[b]		96	93

[a] FWHM reported for the most intense resonances
[b] Experimental data were best represented using a single exponential (i.e., only a single T_1 to describe the 3 and 6 nm H-SiNPs).
[c] NMR surface fraction estimates were based on fitting of direct NMR data
[d] Model surface fraction estimates using geometric calculations based on the SiNP structure described by Zhao et al. and Avramov et al. and informed by Si lattice parameters.[113, 114]

Further exemplifying the combined benefits of preparing well-defined H-SiNPs and evaluating them using NMR spectroscopy, the determination of the nuclear spin lattice relaxation times yields an intriguing size dependence (Table 2). As expected, smaller NPs (d ~ 3 and 6 nm) exhibit shorter T_1 values[9, 48, 53] with a mono-exponential longitudinal magnetization recovery; larger H-SiNPs (d ~ 9, 21, and 64 nm) show bi-exponential recovery (Figure S5). We assign the rapid (i.e., minutes) and slow (i.e., hours) T_1 components of the large NPs to surface and core ^{29}Si species, respectively. To further elucidate the surface of the larger particles, one may select a relaxation time (~ 200 s) which enhances the signal from the surface/subsurface nuclei that have a much shorter T_1 relaxation time (on the order of minutes) than the core nuclei. The differences in T_1 values for the surface vs. core are attributed to the two chemically distinct environments: the disordered surface allows more motion and a larger distribution of Si environments, improving the efficiency of the relaxation, while the core aligns itself into a diamond-like structure with a rigid lattice, impeding relaxation as the particle size increases. Another factor is the presence of unpaired electrons on the

surface (i.e., dangling bonds) would cause a reduction in ^{29}Si spin-lattice relaxation, therefore as the size of the NP increases, the core nuclei become increasingly distant from the surface, resulting in an increase in the experimentally determined nuclear T_1.

CONCLUSIONS

In this work, we present a state-of-the-art multi-faceted approach to characterizing and understanding the atomic-level structure of H-SiNPs. Using a combination of XPS, bright field TEM, XRD, FTIR and ^{29}Si MAS NMR spectroscopy, we probe the complex surface and core structure of H-SiNPs. Solid-state NMR methods allowed us to further interrogate a series of H-SiNPs with dimensions in the range of 3 to 64 nm where three unique structural environments (surface, subsurface and core) were identified. The surface silicon atoms are found between −80 to −120 ppm, while core Si, that become observable in H-SiNPs > 6 nm, exhibit chemical shifts similar to that for bulk silicon. Based upon the present experimental data, strain in the long-range periodicity emerges below 9 nm particles, suggesting a critical size-junction; however, the NMR chemical shifts are dominated by changes to the electronic structure of H-SiNPs. Are SiNPs crystalline to the core? Generally yes, but below 3 nm the definition of order vs. disorder becomes unclear since the number of repeating unit cells becomes limited, further straining the surface structure which makes up the bulk of the particle. The structural insight obtained by this investigation provides invaluable information key to the rational design and development of SiNP-based applications including, but not limited to, sensors, battery electrodes, optical materials, and contrast agents.

ASSOCIATED CONTENT

SUPPORTING MATERIAL

Electronic supplementary information (ESI) available.

Survey XPS data, tabulated elemental composition and peak composition. XPS fitting. Histograms showing size distributions for 3 nm dodecyl-terminated SiNPs, as well as 6, 9, 21 and 64 nm H-SiNPs. XRD alignment with LaB_6 (NIST) and Si standards. T_1 buildup curves for H-SiNPs. FTIR data for H-SiNPs. XRD peak broadening distribution for nanocrystalline materials. Contact time array for ^{29}Si CP MAS NMR. NMR data for oxidized 9 nm H-SiNPs. High resolution XPS of the Si 2p peak and FTIR for the 6 nm H-SiNPs after undertaking the NMR experiments. Deconvolution of NMR data for surface/subsurface. List of common chemical shifts for silicon-containing materials. Estimated Si content in structural components.

AUTHOR INFORMATION

[§]Author Contributions: A.N.T. and M.H. contributed equally to this work.

*Corresponding Authors: Jonathan G. C. Veinot: jveinot@ualberta.ca; Vladimir K. Michaelis: vladimir.michaelis@ualberta.ca

Notes

The authors declare no competing financial interests.

ACKNOWLEDGMENTS

The Natural Sciences and Engineering Research Council (NSERC) of Canada Discovery Grants Program (RGPIN-2015-03896 and 2016-05547) and the University of Alberta are acknowledged for their generous research support. A.N.T. is supported by the Alberta Innovates Graduate Student Scholarship and the Government of Alberta Queen Elizabeth II Graduate Scholarship. M.H. is partially supported by the Government of Alberta Queen Elizabeth II Graduate Scholarship. The ATUMS training program is supported by NSERC CREATE is thanked for continued generous financial support (CREATE-463990-2015).

REFRENCES

1. Union, T. E., Ed. Publications Office of the European Union: Official Journal of the European Union, 2017; Vol. 2017/1975, p 3.
2. Liu, J.; Erogbogbo, F.; Yong, K.-T.; Ye, L.; Liu, J.; Hu, R.; Chen, H.; Hu, Y.; Yang, Y.; Yang, J.; Roy, I.; Karker, N. A.; Swihart, M. T.; Prasad, P. N. Assessing Clinical Prospects of Silicon Quantum Dots: Studies in Mice and Monkeys. *ACS Nano* **2013**, *7*, 7303-7310.
3. Park, J. H.; Gu, L.; von Maltzahn, G.; Ruoslahti, E.; Bhatia, S. N.; Sailor, M. J. Biodegradable Luminescent Porous Silicon Nanoparticles for in vivo Applications. *Nature Mater.* **2009**, *8*, 331-336.
4. Mobarok, M. H.; Purkait, T. K.; Islam, M. A.; Miskolzie, M.; Veinot, J. G. C. Instantaneous Functionalization of Chemically Etched Silicon Nanocrystal Surfaces. *Angew. Chem. Int. Ed.* **2017**, *56*, 6073-6077.
5. Islam, M. A.; Mobarok, M. H.; Sinelnikov, R.; Purkait, T. K.; Veinot, J. G. C. Phosphorus Pentachloride Initiated Functionalization of Silicon Nanocrystals. *Langmuir* **2017**, *33*, 8766-8773.
6. Mastronardi, M. L.; Maier-Flaig, F.; Faulkner, D.; Henderson, E. J.; Kübel, C.; Lemmer, U.; Ozin, G. A. Size-Dependent Absolute Quantum Yields for Size-Separated Colloidally-Stable Silicon Nanocrystals. *Nano Lett.* **2012**, *12*, 337-342.
7. Bhattacharjee, S.; Rietjens, I. M. C. M.; Singh, M. P.; Atkins, T. M.; Purkait, T. K.; Xu, Z.; Regli, S.; Shukaliak, A.; Clark, R. J.; Mitchell, B. S.; Alink, G. M.; Marcelis, A. T. M.; Fink, M. J.; Veinot, J. G. C.; Kauzlarich, S. M.; Zuilhof, H. Cytotoxicity of Surface-Functionalized Silicon and Germanium Nanoparticles: The Dominant Role of Surface Charges. *Nanoscale* **2013**, *5*, 4870-4883.
8. Erogbogbo, F.; Yong, K.-T.; Roy, I.; Hu, R.; Law, W.-C.; Zhao, W.; Ding, H.; Wu, F.; Kumar, R.; Swihart, M. T.; Prasad, P. N. In vivo Targeted Cancer Imaging, Sentinel Lymph Node Mapping and Multi-Channel Imaging with Biocompatible Silicon Nanocrystals. *ACS Nano* **2011**, *5*, 413-423.
9. Cassidy, M. C.; Chan, H. R.; Ross, B. D.; Bhattacharya, P. K.; Marcus, C. M. In vivo Magnetic Resonance Imaging of Hyperpolarized Silicon Particles. *Nature Nanotechnol.* **2013**, *8*, 363-368.
10. Tu, C.; Ma, X.; House, A.; Kauzlarich, S. M.; Louie, A. Y. PET Imaging and Biodistribution of Silicon Quantum Dots in Mice. *ACS Med. Chem. Lett.* **2011**, *2*, 285-288.
11. Liu, X.; Zhao, S.; Gu, W.; Zhang, Y.; Qiao, X.; Ni, Z.; Pi, X.; Yang, D. Light-Emitting Diodes Based on Colloidal Silicon Quantum Dots with Octyl and Phenylpropyl Ligands. *ACS Appl. Mater. Interfaces* **2018**, *10*, 5959-5966.
12. Dutta, M.; Thirugnanam, L.; Van Trinh, P.; Fukata, N. High Efficiency Hybrid Solar Cells Using Nanocrystalline Si Quantum Dots and Si Nanowires. *ACS Nano* **2015**, *9*, 6891-6899.
13. Svrcek, V.; McDonald, C.; Lozac'h, M.; Tayagaki, T.; Koganezawa, T.; Miyadera, T.; Mariotti, D.; Matsubara, K. Stable Ultrathin Surfactant-Free Surface-Engineered Silicon Nanocrystal Solar Cells Deposited at Room Temperature. *Energy Sci. Eng.* **2017**, *5*, 184-193.
14. Zhao, S.; Pi, X. Colloidal Silicon Quantum Dots and Solar Cells. In *Handbook of Photovoltaic Silicon*, Yang, D., Ed. Springer Berlin Heidelberg: Berlin, Heidelberg, 2017; pp 1-27.
15. Gonzalez, C. M.; Veinot, J. G. C. Silicon Nanocrystals for the Development of Sensing Platforms. *J. Mater. Chem. C* **2016**, *4*, 4836-4846.
16. Meinardi, F.; Ehrenberg, S.; Dhamo, L.; Carulli, F.; Mauri, M.; Bruni, F.; Simonutti, R.; Kortshagen, U.; Brovelli, S. Highly Efficient Luminescent Solar Concentrators based on Earth-Abundant Indirect-Bandgap Silicon Quantum Dots. *Nature Photonics* **2017**, *11*, 177-185.
17. Chan, C. K.; Peng, H. L.; Liu, G.; McIlwrath, K.; Zhang, X. F.; Huggins, R. A.; Cui, Y. High-Performance Lithium Battery Anodes using Silicon Nanowires. *Nature Nanotechnol* **2008**, *3*, 31-35.

18. Kim, H.; Seo, M.; Park, M. H.; Cho, J. A Critical Size of Silicon Nano-Anodes for Lithium Rechargeable Batteries. *Angew. Chem. Int. Ed.* **2010**, *49*, 2146-9.
19. Su, X.; Wu, Q.; Li, J.; Xiao, X.; Lott, A.; Lu, W.; Sheldon Brian, W.; Wu, J. Silicon-Based Nanomaterials for Lithium-Ion Batteries: A Review. *Adv. Energy Mater.* **2014**, *4*, 1300882.
20. Dohnalová, K.; Gregorkiewicz, T.; Kůsová, K. Silicon Quantum Dots: Surface Matters. *J. Phys.: Condens Matter* **2014**, *26*, 173201.
21. Chan, C. K.; Ruffo, R.; Hong, S. S.; Cui, Y. Surface Chemistry and Morphology of the Solid Electrolyte Interphase on Silicon Nanowire Lithium-ion Battery Anodes. *J. Power Sources* **2009**, *189*, 1132-1140.
22. Dasog, M.; Yang, Z. Y.; Regli, S.; Atkins, T. M.; Faramus, A.; Singh, M. P.; Muthuswamy, E.; Kauzlarich, S. M.; Tilley, R. D.; Veinot, J. G. C. Chemical Insight into the Origin of Red and Blue Photoluminescence Arising from Freestanding Silicon Nanocrystals. *ACS Nano* **2013**, *7*, 2676-2685.
23. Dasog, M.; De los Reyes, G. B.; Titova, L. V.; Hegmann, F. A.; Veinot, J. G. Size vs Surface: Tuning the Photoluminescence of Freestanding Silicon Nanocrystals across the Visible Spectrum via Surface Groups. *ACS Nano* **2014**, *8*, 9636-9648.
24. Dasog, M.; Bader, K.; Veinot, J. G. C. Influence of Halides on the Optical Properties of Silicon Quantum Dots. *Chem. Mater.* **2015**, *27*, 1153-1156.
25. Wheeler, L. M.; Anderson, N. C.; Palomaki, P. K. B.; Blackburn, J. L.; Johnson, J. C.; Neale, N. R. Silyl Radical Abstraction in the Functionalization of Plasma-Synthesized Silicon Nanocrystals. *Chem. Mater.* **2015**, *27*, 6869-6878.
26. Lee, B. G.; Hiller, D.; Luo, J. W.; Semonin, O. E.; Beard, M. C.; Zacharias, M.; Stradins, P. Strained Interface Defects in Silicon Nanocrystals. *Adv. Funct. Mater.* **2012**, *22*, 3223-3232.
27. Kleovoulou, K.; Kelires, P. C. Stress State of Embedded Si Nanocrystals. *Phys. Rev. B* **2013**, *88*, 085424.
28. Zhou, Z. Y.; Brus, L.; Friesner, R. Electronic Structure and Luminescence of 1.1-and 1.4-nm Silicon Nanocrystals: Oxide Shell Versus Hydrogen Passivation. *Nano Lett.* **2003**, *3*, 163-167.
29. Shu, Y. N.; Kortshagen, U. R.; Levine, B. G.; Anthony, R. J. Surface Structure and Silicon Nanocrystal Photoluminescence: The Role of Hypervalent Silyl Groups. *J. Phys. Chem. C* **2015**, *119*, 26683-26691.
30. Veprek, S.; Sarott, F.; Iqbal, Z. Effect of Grain Boundaries on the Raman Spectra, Optical Absorption, and Elastic Light Scattering in Nanometer-sized Crystalline Silicon. *Phys. Rev. B Condens. Matter* **1987**, *36*, 3344-3350.
31. Nikitin, T.; Khriachtchev, L. Optical and Structural Properties of Si Nanocrystals in SiO_2 Films. *Nanomaterials* **2015**, *5*, 614-655.
32. Yogi, P.; Tanwar, M.; Saxena, S. K.; Mishra, S.; Pathak, D. K.; Chaudhary, A.; Sagdeo, P. R.; Kumar, R. Quantifying the Short-Range Order in Amorphous Silicon by Raman Scattering. *Anal. Chem.* **2018**, *90*, 8123-8129.
33. Marra, D. C.; Edelberg, E. A.; Naone, R. L.; Aydil, E. S. Silicon Hydride Composition of Plasma-Deposited Hydrogenated Amorphous and Nanocrystalline Silicon Films and Surfaces. *J. Vac. Sci. Technol. A* **1998**, *16*, 3199-3210.
34. Mangolini, L.; Kortshagen, U. Plasma-Assisted Synthesis of Silicon Nanocrystal Inks. *Adv. Mater.* **2007**, *19*, 2513-2519.
35. Jariwala, B. N.; Kramer, N. J.; Petcu, M. C.; Bobela, D. C.; Sanden, M. C. M. v. d.; Stradins, P.; Ciobanu, C. V.; Agarwal, S. Surface Hydride Composition of Plasma-Synthesized Si Nanoparticles. *J. Phys. Chem. C* **2011**, *115*, 20375-20379.

36. Zipoli, F.; Bernasconi, M. Ab initio Simulation of the Grafting of Phenylacetylene on Hydrogenated Surfaces of Crystalline Silicon Catalyzed by a Lewis Acid. *J. Phys. Chem. B* **2006**, *110*, 23403-23409.
37. Hua, F.; Swihart, M. T.; Ruckenstein, E. Efficient Surface Grafting of Luminescent Silicon Quantum Dots by Photoinitiated Hydrosilylation. *Langmuir* **2005**, *21*, 6054-6062.
38. Hua, F.; Erogbogbo, F.; Swihart, M. T.; Ruckenstein, E. Organically Capped Silicon Nanoparticles with Blue Photoluminescence Prepared by Hydrosilylation Followed by Oxidation. *Langmuir* **2006**, *22*, 4363-4370.
39. Giuliani, J. R.; Harley, S. J.; Carter, R. S.; Power, P. P.; Augustine, M. P. Using Liquid and Solid-State NMR and Photoluminescence to Study the Synthesis and Solubility Properties of Amine Capped Silicon Nanoparticles. *Solid State Nucl. Magnet. Reson.* **2007**, *32*, 1-10.
40. Shiohara, A.; Prabakar, S.; Faramus, A.; Hsu, C. Y.; Lai, P. S.; Northcote, P. T.; Tilley, R. D. Sized Controlled Synthesis, Purification, and Cell Studies with Silicon Quantum Dots. *Nanoscale* **2011**, *3*, 3364-3370.
41. Zou, J.; Kauzlarich, S. M. Functionalization of Silicon Nanoparticles via Silanization: Alkyl, Halide and Ester. *J. Cluster Sci.* **2008**, *19*, 341-355.
42. Ahire, J. H.; Wang, Q.; Coxon, P. R.; Malhotra, G.; Brydson, R.; Chen, R.; Chao, Y. Highly Luminescent and Nontoxic Amine-Capped Nanoparticles from Porous Silicon: Synthesis and their use in Biomedical Imaging. *ACS Applied Mater. & Inter.* **2012**, *4*, 3285-3292.
43. Biesta, W.; van Lagen, B.; Gevaert, V. S.; Marcelis, A. T. M.; Paulusse, J. M. J.; Nielen, M. W. F.; Zuilhof, H. Preparation, Characterization, and Surface Modification of Trifluoroethyl Ester-Terminated Silicon Nanoparticles. *Chem. Mater.* **2012**, *24*, 4311-4318.
44. Mayeri, D.; Phillips, B. L.; Augustine, M. P.; Kauzlarich, S. M. NMR Study of the Synthesis of Alkyl-Terminated Silicon Nanoparticles from the Reaction of $SiCl_4$ with the Zintl Salt, NaSi. *Chem. Mater.* **2001**, *13*, 765-770.
45. Baldwin, R. K.; Pettigrew, K. A.; Ratai, E.; Augustine, M. P.; Kauzlarich, S. M. Solution Reduction Synthesis of Surface Stabilized Silicon Nanoparticles. *Chem. Commun.* **2002**, *17*, 1822-1823.
46. Carter, R. S.; Harley, S. J.; Power, P. P.; Augustine, M. P. Use of NMR Spectroscopy in the Synthesis and Characterization of Air- and Water-Stable Silicon Nanoparticles from Porous Silicon. *Chem. Mater.* **2005**, *17*, 2932-2939.
47. Yesinowski, J. P. Solid-State NMR of Inorganic Semiconductors. In *Solid State NMR*, Chan, J. C. C., Ed. Springer Berlin Heidelberg: Berlin, Heidelberg, 2012; pp 229-312.
48. Atkins, T. M.; Cassidy, M. C.; Lee, M.; Ganguly, S.; Marcus, C. M.; Kauzlarich, S. M. Synthesis of Long T_1 Silicon Nanoparticles for Hyperpolarized ^{29}Si Magnetic Resonance Imaging. *ACS Nano* **2013**, *7*(2), 1609-1617.
49. Neiner, D.; Kauzlarich, S. M. Hydrogen-Capped Silicon Nanoparticles as a Potential Hydrogen Storage Material: Synthesis, Characterization, and Hydrogen Release. *Chem. Mater.* **2010**, *22*(2), 487-493.
50. El-Demellawi, J. K.; Holt, C. R.; Abou-Hamad, E.; Al-Talla, Z. A.; Saih, Y.; Chaieb, S. Room-Temperature Reactivity Of Silicon Nanocrystals With Solvents: The Case of Ketone and Hydrogen Production From Secondary Alcohols: Catalysis? *ACS Applied Mater. Inter.* **2015**, *7*, 13794-13800.
51. Kravitz, K.; Kamyshny, A.; Gedanken, A.; Magdassi, S. Solid State Synthesis of Water-Dispersible Silicon Nanoparticles from Silica Nanoparticles. *J. Solid State Chem.* **2010**, *183*, 1442-1447.

52. Kolyagin, Y. G.; Zakharov, V. N.; Yatsenko, A. V.; Aslanov, L. A. Studies of Silicon Nanocluster Ligand Coating by Solid-State NMR. *Russian Chem. Bulle.* **2015**, *64*, 1829-1832.
53. Aptekar, J. W.; Cassidy, M. C.; Johnson, A. C.; Barton, R. A.; Lee, M.; Ogier, A. C.; Vo, C.; Anahtar, M. N.; Ren, Y.; Bhatia, S. N.; Ramanathan, C.; Cory, D. G.; Hill, A. L.; Mair, R. W.; Rosen, M. S.; Walsworth, R. L.; Marcus, C. M. Silicon Nanoparticles as Hyperpolarized Magnetic Resonance Imaging Agents. *ACS Nano* **2009**, *3*, 4003-4008.
54. Faulkner, A. R.; DiVerdi, A. J.; Yang, Y.; Kobayashi, T.; Maciel, E. G. The Surface of Nanoparticle Silicon as Studied by Solid-State NMR. *Materials* **2013**, *6*, 18-46.
55. Lee, D.; Kaushik, M.; Coustel, R.; Chenavier, Y.; Chanal, M.; Bardet, M.; Dubois, L.; Okuno, H.; Rochat, N.; Duclairoir, F.; Mouesca, J. M.; De Paëpe, G. Solid-State NMR and DFT Combined for the Surface Study of Functionalized Silicon Nanoparticles. *Chemistry – A European Journal* **2015**, *21*, 16047-16058.
56. Hanrahan, M. P.; Fought, E. L.; Windus, T. L.; Wheeler, L. M.; Anderson, N. C.; Neale, N. R.; Rossini, A. J. Characterization of Silicon Nanocrystal Surfaces by Multidimensional Solid-State NMR Spectroscopy. *Chem. Mater.* **2017**, *29*, 10339-10351.
57. Coleman, N. R. B.; Morris, M. A.; Spalding, T. R.; Holmes, J. D. The Formation of Dimensionally Ordered Silicon Nanowires within Mesoporous Silica. *J. Amer. Chem. Soc.* **2001**, *123*, 187-188.
58. Davidowski, S. K.; Holland, G. P. Solid-State NMR Characterization of Mixed Phosphonic Acid Ligand Binding and Organization on Silica Nanoparticles. *Langmuir* **2016**, *32*, 3253-3261.
59. Lafon, O.; Thankamony, A. S. L.; Kobayashi, T.; Carnevale, D.; Vitzthum, V.; Slowing, I. I.; Kandel, K.; Vezin, H.; Amoureux, J.-P.; Bodenhausen, G.; Pruski, M. Mesoporous Silica Nanoparticles Loaded with Surfactant: Low Temperature Magic Angle Spinning ^{13}C and ^{29}Si NMR Enhanced by Dynamic Nuclear Polarization. *J. Phys. Chem. C* **2013**, *117*, 1375-1382.
60. Sugiyama, Y.; Okamoto, H.; Mitsuoka, T.; Morikawa, T.; Nakanishi, K.; Ohta, T.; Nakano, H. Synthesis and Optical Properties of Monolayer Organosilicon Nanosheets. *J. Amer. Chem. Soc.* **2010**, *132*, 5946-5947.
61. Helbich, T.; Lyuleeva, A.; Höhlein, I. M. D.; Marx, P.; Scherf, L. M.; Kehrle, J.; Fässler, T. F.; Lugli, P.; Rieger, B. Radical-Induced Hydrosilylation Reactions for the Functionalization of Two-Dimensional Hydride Terminated Silicon Nanosheets. *Chem. – A Euro. J.* **2016**, *22*, 6194-6198.
62. Mackenzie, K.; Smith, M. Chapter 4 - ^{29}Si NMR. In *Pergamon Materials Series*, MacKenzie, K. J. D.; Smith, M. E., Eds. Pergamon: 2002; Vol. 6, pp 201-268.
63. Takeuchi, Y.; Takayama, T. ^{29}Si NMR Spectroscopy of Organosilicon Compounds. In *The Chemistry of Organic Silicon Compounds*, 2003; pp 267-354.
64. Wrackmeyer, B. Applications of ^{29}Si NMR Parameters. In *Annual Reports on NMR Spectroscopy*, Webb, G. A., Ed. Academic Press: 2006; Vol. 57, pp 1-49.
65. Harris, R. K.; Kimber, B. J. ^{29}Si NMR as a Tool for Studying Silicones. *Applied Spectroscopy Reviews* **2007**, *10*, 117-137.
66. Collins, W. T. F., C. L. Condensed Soluble Hydrogensilsesquioxane Resin. US3615272A, 1971.
67. Hessel, C. M.; Henderson, E. J.; Veinot, J. G. C. Hydrogen Silsesquioxane: A Molecular Precursor for Nanocrystalline Si−SiO_2 Composites and Freestanding Hydride-Surface-Terminated Silicon Nanoparticles. *Chem. Mater.* **2006**, *18* (26), 6139-6146.
68. Barr, T. L.; Seal, S. Nature of the use of Adventitious Carbon as a Binding Energy Standard. *J. Vac. Sci. Tech. A* **1995**, *13*, 1239-1246.
69. Payne, B. P.; Biesinger, M. C.; McIntyre, N. S. The Study of Polycrystalline Nickel Metal Oxidation by Water Vapour. *J. Elec. Spectros. Rel. Phen.* **2009**, *175*, 55-65.

70. Sublemontier, O.; Nicolas, C.; Aureau, D.; Patanen, M.; Kintz, H.; Liu, X.; Gaveau, M.-A.; Le Garrec, J.-L.; Robert, E.; Barreda, F.-A.; Etcheberry, A.; Reynaud, C.; Mitchell, J. B.; Miron, C. X-Ray Photoelectron Spectroscopy of Isolated Nanoparticles. *J. Phys. Chem. Lett.* **2014**, *5*, 3399-3403.
71. Plymale, N. T.; Dasog, M.; Brunschwig, B. S.; Lewis, N. S. A Mechanistic Study of the Oxidative Reaction of Hydrogen-Terminated Si(111) Surfaces with Liquid Methanol. *J. Phys. Chem. C* **2017**, *121*, 4270-4282.
72. Yang, Z. Y.; Iqbal, M.; Dobbie, A. R.; Veinot, J. G. C. Surface-Induced Alkene Oligomerization: Does Thermal Hydrosilylation Really Lead to Monolayer Protected Silicon Nanocrystals? *J. Amer. Chem. Soc.* **2013**, *135*, 17595-17601.
73. Bruker AXS (2008): TOPAS V4: General Profile and Structure Analysis Software for Powder Diffraction Data. - User's Manual, Bruker AXS, Karlsruhe, Germany.
74. Bennett, A. E.; Rienstra, C. M.; Auger, M.; Lakshmi, K. V.; Griffin, R. G. Heteronuclear Decoupling in Rotating Solids. *J. Chem. Phys.* **1995**, *103*, 6951-6958.
75. Hayashi, S.; Hayamizu, K. Chemical Shift Standards in High-Resolution Solid-State NMR ^{13}C, ^{29}Si, and ^{1}H Nuclei. *Bull. Chem. Soc. Japan* **1991**, *64*, 685-687.
76. Bloch, F. Nuclear Induction. *Phys. Rev.* **1946**, *70*, 460-474.
77. Pines, A.; Gibby, M. G.; Waugh, J. S. Proton-Enhanced Nuclear Induction Spectroscopy. A Method for High Resolution NMR of Dilute Spins in Solids. *J. Chem. Phys.* **1972**, *56*, 1776-1777.
78. Freeman, R.; Hill, H. D. W. Fourier Transform Study of NMR Spin–Lattice Relaxation by "Progressive Saturation". *J. Chem. Phys.* **1971**, *54*, 3367-3377.
79. Hessel, C. M.; Reid, D.; Panthani, M. G.; Rasch, M. R.; Goodfellow, B. W.; Wei, J.; Fujii, H.; Akhavan, V.; Korgel, B. A. Synthesis of Ligand-Stabilized Silicon Nanocrystals with Size-Dependent Photoluminescence Spanning Visible to Near-Infrared Wavelengths. *Chem. Mater.* **2012**, *24*, 393-401.
80. Yu, Y.; Hessel, C. M.; Bogart, T. D.; Panthani, M. G.; Rasch, M. R.; Korgel, B. A. Room Temperature Hydrosilylation of Silicon Nanocrystals with Bifunctional Terminal Alkenes. *Langmuir* **2013**, *29*, 1533-1540.
81. Buriak, J. M. Illuminating Silicon Surface Hydrosilylation: An Unexpected Plurality of Mechanisms. *Chem. Mater.* **2014**, *26*, 763-772.
82. Weeks, S. L.; Macco, B.; van de Sanden, M. C.; Agarwal, S. Gas-phase Hydrosilylation of Plasma-synthesized Silicon Nanocrystals with Short- and Long-chain Alkynes. *Langmuir* **2012**, *28*, 17295-301.
83. Nelles, J.; Sendor, D.; Ebbers, A.; Petrat, F. M.; Wiggers, H.; Schulz, C.; Simon, U. Functionalization of Silicon Nanoparticles via Hydrosilylation with 1-Alkenes. *Colloid. Poly. Sci.* **2007**, *285*, 729-736.
84. Hohlein, I. M.; Kehrle, J.; Helbich, T.; Yang, Z.; Veinot, J. G.; Rieger, B. Diazonium Salts as Grafting Agents and Efficient Radical-Hydrosilylation Initiators for Freestanding Photoluminescent Silicon Nanocrystals. *Chem. Eur. J.* **2014**, *20*, 4212-6.
85. Purkait, T. K.; Iqbal, M.; Wahl, M. H.; Gottschling, K.; Gonzalez, C. M.; Islam, M. A.; Veinot, J. G. Borane-Catalyzed Room-Temperature Hydrosilylation of Alkenes/Alkynes on Silicon Nanocrystal Surfaces. *J. Am. Chem. Soc.* **2014**, *136*, 17914-7.
86. Balzar, D.; Audebrand, N.; Daymond, M. R.; Fitch, A.; Hewat, A.; Langford, J. I.; Le Bail, A.; Louer, D.; Masson, O.; McCowan, C. N.; Popa, N. C.; Stephens, P. W.; Toby, B. H. Size-Strain Line-Broadening Analysis of the Ceria Round-Robin Sample. *J. Appl. Cryst.* **2004**, *37*, 911-924.

87. Hartman, J. S.; Richardson, M. F.; Sherriff, B. L.; Winsborrow, B. G. Magic Angle Spinning NMR Studies of Silicon Carbide: Polytypes, Impurities, and Highly Inefficient Spin-Lattice Relaxation. *J. Amer. Chem. Soc.* **1987**, *109*, 6059-6067.
88. Holzman, G. R.; Lauterbur, P. C.; Anderson, J. H.; Koth, W. Nuclear Magnetic Resonance Field Shifts of Si-29 in Various Materials. *J. Chem. Phys.* **1956**, *25*, 172-173.
89. Reimer, J. A.; Dubois Murphy, P.; Gerstein, B. C.; Knights, J. C. Silicon-29 Cross-Polarization Magic-Angle Sample Spinning Spectra in Amorphous Silicon-Hydrogen Films. *J. Chem. Phys.* **1981**, *74*, 1501.
90. Shao, W.-L.; Shinar, J.; Gerstein, B. C.; Li, F.; Lannin, J. S. Magic-Angle Spinning ^{29}Si NMR Study of Short-Range Order in a-Si. *Phys Rev B* **1990**, *41*, 9491-9494.
91. Bercier, J. J.; Jirousek, M.; Graetzel, M.; Klink, J. J. v. d. Evidence from NMR for Temperature-Dependent Bardeen-Friedel Oscillations in Nanometre-Sized Silver Particles. *J. Phys.: Conden. Matter* **1993**, *5*, L571-L576.
92. Charles, R. J.; Harrison, W. A. Size Effect in Nuclear Magnetic Resonance. *Phys. Rev. Lett.* **1963**, *11*, 75-77.
93. Terskikh, V. V.; Moudrakovski, I. L.; Ratcliffe, C. I.; Ripmeester, J. A.; Reinhold, C. J.; Anderson, P. A.; Edwards, P. P. Size Effects on the Nuclear Magnetic Resonance of Sodium Metal Confined in Controlled Pore Glasses. In *Magnetic Resonance in Colloid and Interface Science*, Fraissard, J.; Lapina, O., Eds. Springer Netherlands: Dordrecht, 2002; pp 469-475.
94. Javadi, M.; Michaelis, V. K.; Veinot, J. G. C. Thermally-Induced Evolution of '$Ge(OH)_2$': Controlling the Formation of Oxide-Embedded Ge Nanocrystals. *J. Phys. Chem. C* **2018**.
95. Cadars, S.; Smith, B. J.; Epping, J. D.; Acharya, S.; Belman, N.; Golan, Y.; Chmelka, B. F. Atomic Positional Versus Electronic Order in Semiconducting ZnSe Nanoparticles. *Phys. Rev. Lett.* **2009**, *103*, 136802.
96. Mobarok, M. H.; Luber, E. J.; Bernard, G. M.; Peng, L.; Wasylishen, R. E.; Buriak, J. M. Phase-Pure Crystalline Zinc Phosphide Nanoparticles: Synthetic Approaches and Characterization. *Chem. Mater.* **2014**, *26*, 1925-1935.
97. Ratcliffe, C. I.; Yu, K.; Ripmeester, J. A.; Badruz Zaman, M.; Badarau, C.; Singh, S. Solid State NMR Studies of Photoluminescent Cadmium Chalcogenide Nanoparticles. *Phys. Chem. Chem. Phys.* **2006**, *8*, 3510-3519.
98. Tomaselli, M.; Yarger, J. L.; Bruchez, M.; Havlin, R. H.; deGraw, D.; Pines, A.; Alivisatos, A. P. NMR Study of InP Quantum Dots: Surface Structure and Size Effects. *J. Chem. Phys.* **1999**, *110*, 8861-8864.
99. Marbella, L. E.; Millstone, J. E. NMR Techniques for Noble Metal Nanoparticles. *Chem. Mater.* **2015**, *27*, 2721-2739.
100. Maciel, G. E.; Sindorf, D. W. Silicon-29 NMR Study of the Surface of Silica Gel by Cross Polarization and Magic-Angle Spinning. *J. Amer. Chem. Soc.* **1980**, *102*, 7606-7607.
101. Hayashi, S.; Hayamizu, K.; Yamasaki, S.; Matsuda, A.; Tanaka, K. Interpretation of ^{29}Si Nuclear Magnetic Resonance Spectra of Amorphous Hydrogenated Silicon. *J. Appl. Phys.* **1986**, *60*, 1839-1841.
102. Hayashi, S.; Hayamizu, K.; Yamasaki, S.; Matsuda, A.; Tanaka, K. ^{29}Si Nuclear Magnetic Resonance of Amorphous Hydrogenated Silicon and Amorphous Microcrystalline Mixed-Phase Hydrogenated Silicon. *Phys. Rev. B* **1987**, *35*, 4581-4590.
103. Pietraβ, T.; Bifone, A.; Roth, R. D.; Koch, V. -P.; Alivisatos, A. P.; Pines, A., ^{29}Si High Resolution Solid State Nuclear Magnetic Resonance Spectroscopy of Porous Silicon. *J. Non-Cryst. Solids* **1996**, *202,* 68-76.

104. Hayashi, S.; Hayamizu, K.; Yamasaki, S.; Matsuda, A.; Tanaka, K. Silicon-29 Nuclear Magnetic Resonance Study of Amorphous-Microcrystalline Mixed-Phase Hydrogenated Silicon. *Japanese J. Applied Phys.* **1986**, *25*, L313-L315.
105. Smith, J. V.; Blackwell, C. S. Nuclear Magnetic Resonance of Silica Polymorphs. *Nature* **1983,** *303*, 223-225.
106. Wang, M.; Wu, X.-P.; Zheng, S.; Zhao, L.; Li, L.; Shen, L.; Gao, Y.; Xue, N.; Guo, X.; Huang, W.; Gan, Z.; Blanc, F.; Yu, Z.; Ke, X.; Ding, W.; Gong, X.-Q.; Grey, C. P.; Peng, L. Identification of Different Oxygen Species in Oxide Nanostructures with ^{17}O Solid-State NMR Spectroscopy. *Sci. Advances* **2015**, *1*, 1-8.
107. Jameson, C. J.; Gutowsky, H. S. Calculation of Chemical Shifts. I. General Formulation and the Z Dependence. *J Chem. Phys.* **1964**, *40*, 1714-1724.
108. Ramsey, N. F. Magnetic Shielding of Nuclei in Molecules. *Phys. Rev.* **1950**, *78*, 699-703.
109. Thayer, A. M.; Steigerwald, M. L.; Duncan, T. M.; Douglass, D. C. NMR Study of Semiconductor Molecular Clusters. *Phys. Rev. Lett.* **1988**, *60*, 2673-2676.
110. Bawendi, M. G.; Carroll, P. J.; Wilson, W. L.; Brus, L. E. Luminescence Properties of CdSe Quantum Crystallites: Resonance Between Interior and Surface Localized States. *J. Chem. Phys.* **1992**, *96*, 946-954.
111. Colvin, V. L.; Alivisatos, A. P.; Tobin, J. G. Valence-Band Photoemission from a Quantum-Dot System. *Phys. Rev. Lett.* **1991**, *66*, 2786-2789.
112. Comedi, D.; Zalloum, O. H. Y.; Irving, E. A.; Wojcik, J.; Roschuk, T.; Flynn, M. J.; Mascher, P. X-Ray Diffraction Study of Crystalline Si Nanocluster Formation in Annealed Silicon-Rich Silicon Oxides. *J. Appl. Phys.* **2006**, *99*, 023518.
113. Zhao, Y.; Kim, Y.-H.; Du, M.-H.; Zhang, S. B. First-Principles Prediction of Icosahedral Quantum Dots for Tetravalent Semiconductors. *Phys. Rev. Lett.* **2004**, *93*, 015502.
114. Avramov, P. V. F., D. G.; Sorokin, P. B.; Chernozatonskii, L. A.; Gordon, M. S. New Symmetric Families of Silicon Quantum Dots and Their Conglomerates as a Tunable Source of Photoluminescence in Nanodevices. *Los Alamos Natl. Lab, Prepr. Arch., Condens. Matter* **2007**, 1-19.
115. Okada, Y.; Tokumaru, Y. Precise Determination of Lattice Parameter and Thermal Expansion Coefficient of Silicon Between 300 and 1500 K. *J Appl Phys* **1984**, *56*, 314-320.

TOC Graphic